Ecotoxicology and Environmental Safety 303 (2025) 118834

Contents lists available at ScienceDirect

Ecotoxicology and Environmental Safety

journal homepage: www.elsevier.com/locate/ecoenv

Revealing 1,3-diphenylpropane's coagulation toxicity via infomaxnet-based network toxicology and molecular simulations

Yan Pan [a,b,d,1], Hongxia Cai [a,b,d,1], Yufeng Ran [c], Hexiang Qiu [d], Zhihang Huang [a,d], Dan Wu [d], Wenjing Zhang [b], Nan Zhang [b], Lei Cheng [d], Juan Long [e], Shan Gao [b], Xiaowei Qiu [c,*], Guojun Li [b,f,**], Bo Xian [a,d,***]

[a] Department of Neurology, Sichuan Provincial People's Hospital, School of Medicine, University of Electronic Science and Technology of China, Chengdu 610072, China
[b] Institute for Toxicology, Beijing Center for Disease Prevention and Control, Beijing 100013, China
[c] Beijing Lepu Diagnostic Technology Co., Ltd., Beijing 102299, China
[d] Laboratory of Aging Research, School of Medicine, University of Electronic Science and Technology of China, Chengdu 611731, China
[e] Department of Laboratory Medicine, Sichuan Academy of Medical Sciences and Sichuan Provincial People's Hospital, School of Medicine, University of Electronic Science and Technology of China, Chengdu, Sichuan 610072, China
[f] School of Public Health, Capital Medical University, Beijing 100069, China

ARTICLE INFO

Edited by Dr. Hao Zhu

Keywords:
Polystyrene dimer
Network toxicology
Deep learning
InfomaxNet
Coagulation function
Molecular dynamics simulation

ABSTRACT

The pervasive use of plastic products has led to environmental contamination by compounds like 1,3-diphenylpropane (SD-1), a polystyrene dimer found in plastic food containers that poses potential health risks. SD-1 can induce coagulation disorder, however, the toxic mechanisms of SD-1 has not been elucidated yet. This study proposes a network toxicology analysis framework—InfomaxNet, which successfully addresses the challenge of lacking prior biological knowledge by analyzing complex biological networks using only network topology. Using the deep learning model MolTrans to predict SD-1 targets, InfomaxNet identified the critical proteins AKT2 and F9. Molecular dynamics simulations revealed that the binding of SD-1 to F9 (FIXa) induces conformational anomalies in its active site, disrupting protein function and increasing the risk of coagulation disorders. *In vitro* experiments confirmed that SD-1 interferes with coagulation pathways involving F9. Subsequently, acute toxicity experiments in *Caenorhabditis elegans* and RT-qPCR validated the impact of SD-1 on AKT2 and its downstream signaling pathways. This study introduces the InfomaxNet framework and applies it to network toxicology analysis, combining deep learning and molecular dynamics simulations to uncover the toxic mechanisms of SD-1 on the coagulation system by pinpointing the peptidase domain of F9, providing new insights for toxicological studies of novel pollutants.

1. Introduction

The widespread production and use of plastic products have created significant global environmental and public health challenges (Megill et al., 2024). Among common plastics, polystyrene (PS) is particularly prevalent in food packaging and disposable containers (Zhang et al., 2023). During PS manufacturing and use, chemical by-products such as styrene oligomers (SOs) are generated, with styrene dimers (SD) and trimers (ST) being the most frequently detected and environmentally persistent forms (Rowdhwal and Chen, 2018).

These oligomers are characterized by their chemical stability and resistance to natural degradation, resulting in persistent contamination of aquatic ecosystems and the potential for these substances to migrate into the human body through food packaging (Rowdhwal and Chen, 2018). Consequently, they pose considerable health risks (Morandi et al., 2021). Among these oligomers, 1,3-Diphenylpropane (Styrene

* Corresponding author.
** Corresponding author at: Institute for Toxicology, Beijing Center for Disease Prevention and Control, Beijing 100013, China.
*** Corresponding author at: Department of Neurology, Sichuan Provincial People's Hospital, School of Medicine, University of Electronic Science and Technology of China, Chengdu 610072, China.
E-mail addresses: xiaowei_qiu@leputechnology.com (X. Qiu), ligj@bjcdc.org (G. Li), xianbo@uestc.edu.cn (B. Xian).
[1] Authors contributed equally to this work.

https://doi.org/10.1016/j.ecoenv.2025.118834
Received 15 April 2025; Received in revised form 22 July 2025; Accepted 5 August 2025

Dimer-1, SD-1), a notable polystyrene dimer, has been detected in various environmental and biological samples (Ajaj et al., 2021; Beneventi et al., 2022; Nakai et al., 2014 Nov 15). Its toxicological effects have increasingly attracted the attention of the scientific community, underscoring the need for comprehensive studies on its impact (Hong et al., 2016; Tian et al., 2020).

However, the molecular toxic mechanisms of SD-1 remain unclear, particularly its impact on the coagulation system in mammals. While traditional toxicological methods primarily rely on *in vitro* cell experiments and *in vivo* animal models (Liu et al., 2023a, 2023b) have provided valuable toxicity data, they face significant limitations in systematically elucidating multi-level mechanisms due to their long experimental cycles, high costs, and inherent biological complexity (Zhihang et al., 2024).

To overcome these limitations and achieve a more comprehensive understanding of SD-1's toxicological profile, new computational approaches are needed that can integrate multiple levels of biological information.

Network toxicology has emerged as a powerful paradigm that combines systems biology with computational toxicology (Del Giudice et al., 2024). This approach enables the construction of multi-layered networks encompassing chemicals (Zhao et al., 2023), targets, pathways, and diseases, thereby providing a systems-level perspective on chemical-biological interactions (Huang, 2024). Particularly promising is the integration of deep learning technologies (Kriegeskorte and Golan, 2019), which offer unprecedented capabilities for analyzing complex network data (Ruiz-Garcia et al., 2021). Among these, Graph Neural Networks (GNNs) have shown remarkable success in handling biological network data due to their ability to process non-Euclidean spatial relationships (Bessadok et al., 2023; Veličković, 2023) and capture high-order network features (Wu et al., 2021; Bianchi et al., 2022).

Despite these advances, current GNN implementations face a critical challenge when applied to real-world biological networks: their heavy dependence on abundant node features and label information (Liu et al., 2022a; Xiao et al., 2023). This represents a significant limitation since such detailed data are frequently unavailable for protein-protein interaction (PPI) networks and other biological systems where incomplete information is the norm rather than the exception (Morgan et al., 2023).

To bridge this gap, we developed InfomaxNet, an innovative framework that combines Multi-Scale Deep Graph Infomax (DGI) (Zhou et al., 2023; Liu et al., 2022b) with Edge Weight Learning (EWL) (Sludds et al., 2022). This approach uniquely enables accurate identification of key genes and proteins using only edge list data, thereby eliminating the dependency on node features and labels that has constrained previous methods.

The innovation of InfomaxNet lies in its ability to extract meaningful insights solely from network topology (Momennejad, 2022; Arancibia and Morin, 2022). Additionally, the framework learns the weights of each edge through Edge Weight Learning, identifying crucial protein interactions within the PPI network. This dynamic edge weighting provides a new dimension for key protein identification, highlighting the most significant interactions without requiring explicit node attributes. By overcoming the traditional reliance on node features, InfomaxNet offers a new perspective and powerful tool for analyzing complex biological networks, facilitating a deeper understanding of chemical impacts on biological systems.

In this study, we first utilized the deep learning model MolTrans to predict the targets of SD-1 and constructed the potential target PPI network of SD-1. Subsequently, the InfomaxNet framework was applied to analyze each MCODE cluster of the PPI network, identifying the key proteins AKT2 and F9. To validate the model predictions, Then, acute and chronic toxicity experiments were conducted using the model organism (*C. elegans*). Additionally, real-time quantitative PCR (RT-qPCR) was employed to assess the impact of SD-1 on AKT2 and its downstream signaling pathways.

Molecular dynamics simulations were first performed to explore the interaction mechanism between SD-1 and the F9 protein. The simulation results indicated that the binding of SD-1 to the F9 protein induces conformational changes in its active site, potentially disrupting F9's normal function. To validate these findings, we conducted *in vitro* thromboelastometry (TEG) and activated partial thromboplastin time (APTT) experiments. The experimental results confirmed that SD-1 significantly affects coagulation function, suggesting that it may impair the function of the coagulation factor F9, thereby increasing the risk of coagulation disorders.

Through the proposed InfomaxNet framework combined with experimental validation and molecular simulations, we systematically elucidates the toxic mechanisms of SD-1. This not only provides scientific evidence for the risk assessment of SD-1 but also offers a replicable research paradigm for the toxicity prediction and mechanistic study of novel pollutants.

2. Methods and materials

2.1. Compound-target interaction prediction using MolTrans

We utilized a machine learning approach, the Molecular Interaction Transformer (MolTrans), to predict drug-target interactions. MolTrans overcomes the shortcomings of traditional DTI prediction models by incorporating a knowledge-based substructural pattern mining algorithm and an interaction modeling module.

The entire workflow was executed on a system equipped with an NVIDIA GPU Tesla P40, utilizing the nvidia-cudnn-cu12 (8.9.2.26) library to optimize deep learning computations. The computational environment was managed using mamba (1.5.8). The model was implemented and executed using the following software and library versions: mamba (1.5.8), numpy (1.26.4), nvidia-cudnn-cu12 (8.9.2.26), pandas (2.2.2), scikit-learn (1.5.1), and torch (2.2.2).

We employed the processed BindingDB dataset as our training, validation, and testing ground. To ensure a robust evaluation, we split the data into a 7:1:2 ratio for training, validation, and testing sets, respectively. Adhering to the established MolTrans methodology, we found that 50 epochs were sufficient for optimal model performance. All results reported in this study were derived from a model trained for 50 epochs.

Then, we fetched the 9606.protein.info.v12.0 from the STRING database and extracted the sequences in FASTA format for each protein. These sequences were then input into the model alongside the SMILES strings of small molecules, which were sourced from the PubChem database. Finally, we calculated the Confidence scores.

2.2. InfomaxNet framework

2.2.1. Data acquisition and graph construction

The protein-protein interaction (PPI) data utilized in this study were sourced from publicly available databases and formatted as a tab-separated values (TSV) file. Each edge in the dataset represented an interaction between two proteins as defined in the PPI data. To prepare the PPI network for analysis with PyTorch Geometric, the edge list was converted into an edge index tensor with a shape of *[2, E]*, where *E* denotes the number of edges. In the absence of detailed node features, an identity matrix was employed as the node feature matrix, resulting in a tensor of shape *[N, N]*, where *N* represents the number of nodes. This approach ensures that each node is uniquely identifiable without introducing additional feature complexity. The prepared data was then encapsulated within a PyTorch Geometric Data object, facilitating seamless integration with subsequent deep learning models.

2.2.2. Framework architecture

The InfomaxNet framework comprises a Multi-Scale Encoder, the Deep Graph Infomax (DGI) model, and an Edge Weight Learning (EWL) module. The Multi-Scale Encoder consists of multiple layers of Graph

Convolutional Networks (GCNs), each designed to capture both local and global structural features of the PPI network. Specifically, the encoder begins with an input layer that processes the node feature matrix and edge indices, followed by several hidden GCN layers with a hidden dimension size of 64. Each GCN layer is succeeded by a Parametric ReLU (PreLU) activation function to introduce non-linearity and enhance the model's expressive capacity.

The DGI model employs a contrastive learning approach to extract high-quality node embeddings from the network. It processes both the original and a corrupted version of the node feature matrix, where the latter is generated by randomly shuffling the node features to disrupt the original network structure. The encoder generates embeddings for both the original and corrupted graphs, and a global summary vector is derived from the embeddings of the original graph through a mean pooling operation followed by a sigmoid activation. Mathematically, the global summary vector s is defined as:

$$s = \sigma(\frac{1}{N}\sum_{i=1}^{N} \boldsymbol{z_i})$$

where $\boldsymbol{Z_i}$ represents the embedding of node i, and σ denotes the sigmoid function. The DGI model then maximizes the mutual information between the node embeddings of the original graph and the global summary while minimizing it for the corrupted graph. This objective can be formulated as:

$$\mathscr{L}_{DGI} = -\frac{1}{N}\sum_{i=1}^{N}\left(\log\sigma(\boldsymbol{z_i}\cdot s) + \log\sigma\left(-\boldsymbol{z_i'}\cdot s\right)\right)$$

where $\boldsymbol{z_i}$ are the embeddings from the corrupted graph.

The EWL module assigns learnable weights to each edge in the PPI network, reflecting the significance of each protein interaction. Initially, all edge weights are set to one and treated as learnable parameters. During training, these weights are dynamically adjusted through backpropagation to highlight the most critical interactions. The weights are constrained to be positive using a softplus activation function and normalized to lie between 0 and 1, ensuring that the weights accurately represent the relative importance of each interaction. The normalization process can be expressed as:

$$w_{\text{norm},e} = \frac{\text{softplus}(w_e)}{\max(\text{softplus}(\boldsymbol{w}))}$$

Where w_e is the raw weight for edge e, and $softplus(x) = \ln(1 + e^x)$.

2.2.3. Model training

A fixed random seed was set to guarantee reproducibility of the results. The loss function employed was the DGI loss, which aims to maximize the mutual information between the node embeddings of the original graph and the global summary while minimizing it for the corrupted graph. The Adam optimizer was utilized with a learning rate of 0.001 and a weight decay of 5e-4, optimizing both the model parameters and the edge weights.

The training process spanned 200 epochs, during which the model alternately updated the edge weights and the encoder parameters. In each epoch, the edge weights were first normalized using the softplus function followed by a scaling step to ensure they remained within the [0, 1] range. The node features were then corrupted by randomly shuffling them, and both the original and corrupted graphs were passed through the DGI model to obtain their respective embeddings and global summaries. The DGI loss was computed based on these embeddings, and gradients were backpropagated to update the model and edge weight parameters. Loss values were logged every 10 epochs and at the first epoch to monitor the training progress.

2.2.4. Post-processing and key node identification

Upon completion of the training phase, the model was switched to evaluation mode to extract the final node embeddings and edge weights without further parameter updates. The normalized edge weights were obtained using the same softplus and normalization procedure as during training. The node embeddings were computed by passing the original node features and edge indices through the trained encoder. The importance of each node was quantified by calculating the norm of its embedding vector, providing an importance score that reflects the node's significance within the network. Mathematically, the importance score I_i for node i is given by:

$$I_i = |\boldsymbol{z_i}|_2$$

To complement the embedding-based importance scores, traditional centrality measures were also computed using NetworkX. These included Degree Centrality, Betweenness Centrality, and Eigenvector Centrality, each offering a different perspective on node importance based on connectivity, information flow, and influence within the network, respectively. The centrality measures were normalized and combined with the DGI-derived importance scores to generate a comprehensive combined score for each node. The combined score C_i was calculated as:

$$C_i = \frac{I_i + EC_i}{2}$$

Where EC_i represents the Eigenvector Centrality of node i. This combined score facilitated a better ranking of key proteins by integrating both embedding-based and traditional network metrics.

2.3. Molecular dynamics analysis

The starting structure of the SD1-F9 complex was obtained from docking studies (see 2.2). The protein structure was downloaded from the Protein Data Bank (PDB) in PDB format. Hydrogen atoms were added, and the protonation states of the titratable residues were assigned using the PDB2PQR server (https://server.poissonboltzmann.org/pdb2pqr) with default settings. The complex was placed in a cubic box and solvated using a TIP3P water model, ensuring at least 1.0 nm between the complex and the box edges.

Molecular dynamics (MD) simulations were performed using GROMACS 2022.3 software. The CHARMM36 force field, along with the TIP3P water model, was applied to represent the system. Before running the MD simulation, energy minimization was done in two steps. First, only the solvent molecules were minimized while the protein and ligand were restrained with a harmonic potential (force constant of 1000 kJ/mol/nm^2). Then, a full system minimization was conducted without restraints.

The MD simulations were run in the NPT ensemble (constant pressure and temperature). A Berendsen barostat was used to maintain the pressure at 1 atm with a coupling constant of 1 ps, and the temperature was set at 310 K using a velocity-rescale thermostat with a coupling constant of 0.1 ps. Periodic boundary conditions were applied, and long-range electrostatic interactions were calculated using the Particle Mesh Ewald (PME) method with a real space cutoff of 1.0 nm. Lennard-Jones interactions had a cutoff of 1.0 nm, with a smooth switching function applied from 0.9 to 1.0 nm. The LINCS algorithm was used to constrain all bonds involving hydrogen atoms.

The production phase of the MD simulation was typically run for 100 nanoseconds with a time step of 2 femtoseconds. Coordinates, velocities, and energy data were saved every 10 picoseconds for later analysis.

2.4. Maintenance and experimental setup for C. elegans

2.4.1. Culturing worms and treatment with SD-1

Wild-type *C. elegans* strain N2, procured from the *Caenorhabditis Genetics Center* (Minneapolis, MN, USA), was propagated on a nematode growth medium (NGM). The NGM was prepared by combining 3 g of

NaCl, 2.5 g of BactoPeptone, and 20 g of Agar in 1 L of double-distilled water (ddH_2O). After autoclaving the NGM, it is cooled to 55 °C-60 °C (when the bottle can be comfortably handled), and at this point, 25 ml of PPB, 1 ml of 1 M $MgSO_4$, and 1 ml of 1 M $CaCl_2$ along with cholesterol solution (5 mg/ml) are added and thoroughly mixed.

The worms were synchronized using a standard bleach method. This synchronization involved a mixture of distilled water, 5 M NaOH, and 10 % sodium hypochlorite (NaClO), effectively isolating eggs from adult worms.

In addition to cultivation on solid media, the N2 strain can also be cultured in liquid media using S medium, which supports better dispersal and growth for certain experimental setups. The preparation of S Basal for 1 L of S medium includes dissolving 5.86 g of NaCl, either 1.31 g of K_2HPO_4·3 H_2O or 0.86 g of K_2HPO_4, and 6 g of KH_2PO_4. Post-dissolution. This mixture is subsequently autoclaved to ensure sterility. After cooling, additional components are introduced to complete the S medium formulation: 10 ml of 1 M potassium citrate (pH adjusted to 6.0 with citric acid), 10 ml of trace metals solution, 3 ml of 1 M $CaCl_2$, and 3 ml of 1 M $MgSO_4$, which are essential for maintaining optimal ionic balance and worm health. All of the above reagents were purchased from Solarbio (Beijing, China). N2 were treated with 0.01 % SD-1 (1/10th of LC25) for 2-day chronic exposure experiments.

2.4.2. RT-qPCR analysis

For quantitative real-time PCR (RT-qPCR) analysis, total RNA was extracted from worms using the TRIzol reagent (Tsingke, Beijing, China) according to the manufacturer's instructions. The integrity and concentration of RNA were assessed using a NanoDropONE (Thermo Fisher Scientific, MA, USA). Complementary DNA (cDNA) was synthesized from 1 μg of total RNA using a reverse transcription kit (Tsingke, Beijing, China) following the protocol provided.

RT-qPCR was performed using a SYBR Green PCR Master Mix (Tsingke, Beijing, China) on a real-time PCR system (QuantStudio 3, Thermo Fisher Scientific,Waltham, MA, USA). The thermal cycling conditions were as follows: initial denaturation at 95 °C for 10 min, followed by 40 cycles of 95 °C for 15 s, and 60 °C for 1 min. Each sample was run in triplicate to ensure the accuracy and reproducibility of the results.

Gene-specific primers were used to amplify target genes related to aging and stress response pathways. The expression levels of the genes were normalized to the housekeeping gene actin. Relative gene expression was calculated using the $2^{\Delta\Delta CT}$ method, which provides a quantitative measure of the relative abundance of target mRNA in the samples.

All primers used in the RT-qPCR experiments are listed in Table S1 and are available for reference. This table provides detailed sequences and annealing temperatures for each primer pair, ensuring the transparency and reproducibility of the experimental conditions.

2.5. In vitro tests of blood clotting function

2.5.1. Activated partial thromboplastin time (APTT) tests

This study was approved by the Ethical Committee of the University of Electronic Science and Technology of China, Chengdu, China (Ethics Approval No. 106142025022332068). All procedures followed the ethical guidelines of the Declaration of Helsinki. Written informed consent was obtained from all participants. We utilized activated partial thromboplastin time (APTT) tests to evaluate the impact of varying concentrations of SD-1 on blood clotting function. The APTT analyses were performed using a Sysmex CS-5100 fully automated coagulation analyzer, manufactured by Sysmex Corporation, Japan. The reagents used were from the Sysmex APTT Test Kit (Turbidimetric Method). Fresh citrated whole blood samples were collected from healthy individuals who had not taken any anticoagulant medications, and pure SD-1 liquid was used as the interfering reagent. Prior to participation, all subjects were provided with comprehensive information about the study's objectives, procedures, potential risks, and benefits. Written informed consent was obtained from each participant to ensure their voluntary involvement.

Different concentrations of SD-1 were added to 3000 μL of fresh whole blood, ensuring the total volume of each sample remained at 3000 μL: 0 % (control) with 0 μL of SD-1, 0.01 % with 0.3 μL, 0.05 % with 1.5 μL, 0.1 % with 3 μL, 0.2 % with 6 μL, 0.5 % with 15 μL, 1 % with 30 μL, and 2 % with 60 μL. The samples were gently mixed by inverting the tubes for 5 min to ensure thorough mixing of SD-1 with the blood. After mixing, 200 μL of the mixed whole blood sample was transferred into the turbidimetric cups, and the test was performed in triplicate. The Sysmex CS-5100 fully automated coagulation analyzer was set up according to the manufacturer's instructions, and the APTT values were recorded after the test. It is important to note that the mixing time of SD-1 with the blood sample was strictly controlled to 5 min, and all test parameters were prepared before starting the mixing process.

Additionally, the use of pure SD-1 liquid as the interfering reagent was evaluated for safety, and appropriate measures were taken to handle and dispose of all reagents in accordance with safety guidelines. No adverse effects were reported by the participants during or after the blood collection process.

2.5.2. Thromboelastography (TEG) analyses

We also utilized thromboelastography (TEG) to evaluate the impact of varying concentrations of SD-1 on blood clotting function. The TEG analyses were performed using a CFMS LEPU-8880 thromboelastograph, manufactured by Beijing Lepu Diagnostic Technology Co., Ltd. The reagents used were from the Thromboelastography (Standard Cup) Test Kit (Viscosity Method). Fresh citrated whole blood samples were collected from healthy individuals who had not taken any anticoagulant medications, and pure SD-1 liquid was used as the interfering reagent.

Different concentrations of SD-1 (ranging from 0 % to 10 %) were initially added to 3000 μL of whole blood to perform Activated Partial Thromboplastin Time (APTT) assays. Specifically, SD-1 concentrations of 0 %, 0.1 %, 1 %, 2 %, 5 %, and 10 % were tested across three different batches (utilizing distinct blood samples and separately prepared samples), each with three technical replicates. The average values from the three independent experiments were calculated and presented as N = 3 in the figures. Based on the APTT results, the TEG tests were conducted using SD-1 concentrations starting from the lowest concentration that showed significant effects in the APTT assay (2 %), and included 0.01 %, 0.05 %, 0.1 %, 0.2 %, 0.5 %, 1 %, and 2 %.

For the TEG assays, 3000 μL of blood was supplemented with the specified concentrations of SD-1. The blood and SD-1 mixtures were gently inverted for 5 min to ensure thorough mixing, adhering strictly to the controlled mixing time as a precaution. Following mixing, the TEG was prepared according to the manufacturer's instructions, and the test parameters were configured accordingly. Subsequently, 1 ml of the mixed whole blood sample was transferred into each of three reagent bottles containing Reagent 1, which were gently inverted five times and allowed to stand for 4 min to activate the blood. Next, 20 μL of Reagent 2 was added to the bottom of each test cup, followed by the addition of 340 μL of the activated blood from the reagent bottles to initiate the test. Each group was tested in parallel with six samples. The clotting process was monitored for approximately 30 min until the Maximum Amplitude (MA) signal ceased. Upon completion of the tests, the parameters R, K, angle, and MA values were recorded for analysis.

All procedures were meticulously standardized to ensure consistency and reliability of the results, with SD-1 mixing time strictly controlled and all test parameters prepared prior to the mixing process.

3. Results and discussions

3.1. Target PPI Network of SD-1

Using the MolTrans model, 360 potential targets of Styrene Dimer-1 (SD-1) were predicted (Fig. 2A-B). Among these targets, the study specifically focused on those related to neurotoxicity, coagulation and cytokines.

Out of the 360 predicted targets, 273 were associated with the nervous system according to the GeneCards database, and 132 were related to the coagulation system. These targets encompass roles in neuroinflammation, neurodegenerative diseases, coagulation, and neurovascular functions, highlighting the potential risks that SD-1 may pose to neuronal health, particularly concerning neurocoagulation disorders.

A Protein-Protein Interaction (PPI) network was constructed from these 273 neuro-related targets (Fig. 2C). The network comprised 2594 edges, with an average of 19.652 neighbors per node, indicating a highly interconnected network.

The diameter of the network was calculated to be 5, with a radius of 3, reflecting the longest and shortest paths across the network, respectively. The characteristic path length was 2.455, suggesting that, on average, nodes in the network are separated by approximately two steps. A clustering coefficient of 0.473 was observed, indicating a moderately high level of clustering, where nodes tend to form tightly-knit groups. The network density, a measure of the proportion of potential connections that are actual connections, was 0.075, and the heterogeneity of the network was 0.888, reflecting some variability in the connectivity of nodes.

Furthermore, the network centralization was calculated at 0.358, suggesting the presence of a few highly connected hub nodes. Finally, the network consisted of 3 connected components, meaning that most of the nodes were part of one large interconnected network.

Through MCODE submodule analysis, the most critical clusters in the PPI network were identified. The top three MCODE clusters were subjected to Gene Ontology (GO) Biological Process and KEGG pathway enrichment analyses. The results revealed that the first MCODE cluster is primarily associated with G-protein coupled receptor activity related to the nervous system.

The second MCODE cluster was enriched in metabolic processes and responses to chemical stimuli. Both the first and third MCODE clusters showed strong connections to calcium ion signaling, a critical pathway for neural function and communication (Fig. 2D).

Next, molecular docking simulations were performed. It is well-known that, under certain conditions, polystyrene (PS) can release not only SD-1 but also other styrene dimers (SDs) and trimers (STs). Given their structural similarities, molecular docking was conducted for all recognized SD and ST structures against the protein structures identified in the top three MCODE clusters. The docking results showed that most SD-1 targets had binding affinities lower than −5 kcal/mol, indicating the potential for tight binding. Notably, we found that certain ST compounds exhibited even higher binding affinities for the same proteins compared to SDs, suggesting that STs may pose an even greater risk of neurotoxicity under similar exposure conditions.

3.2. InfomaxNet analysis of each MCODE cluster

To systematically identify the most critical genes in each MCODE cluster, we applied the InfomaxNet framework (Fig. 3A–D). This framework integrates multi-scale graph convolutional encoding, Deep Graph Infomax (DGI), and edge weight learning (EWL) to analyze the structural patterns within the PPI network. The goal is to capture essential interactions and extract high-quality embeddings that

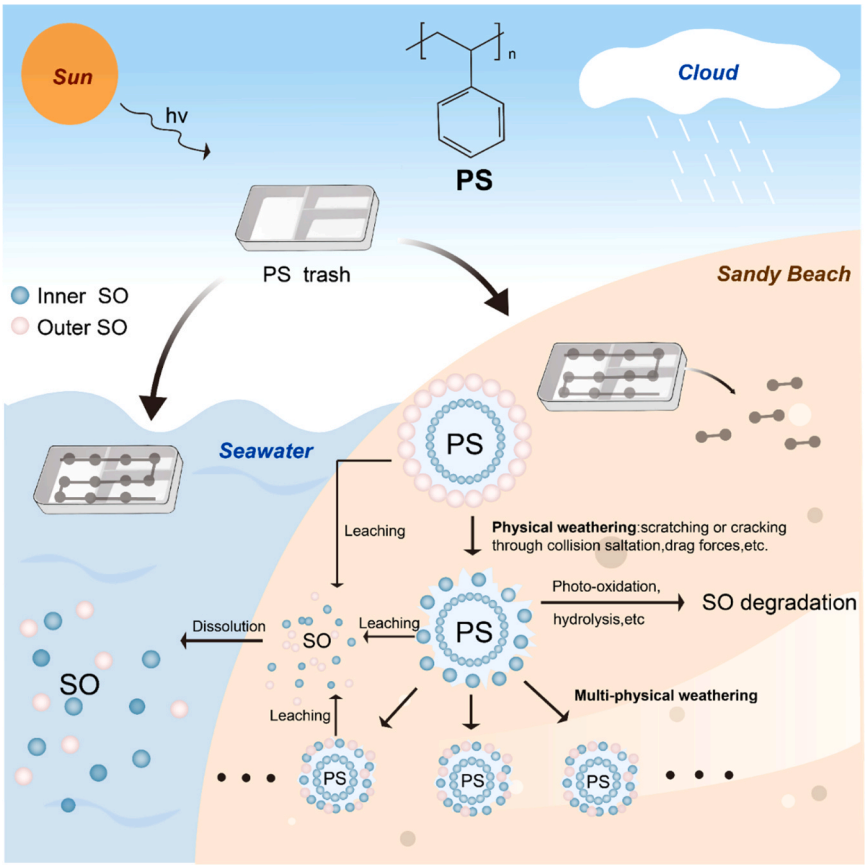

Fig. 1. Environmental degradation and release of styrene oligomers (SO) from polystyrene (PS) waste through physical weathering, leaching, and photodegradation, posing ecological and health risks.

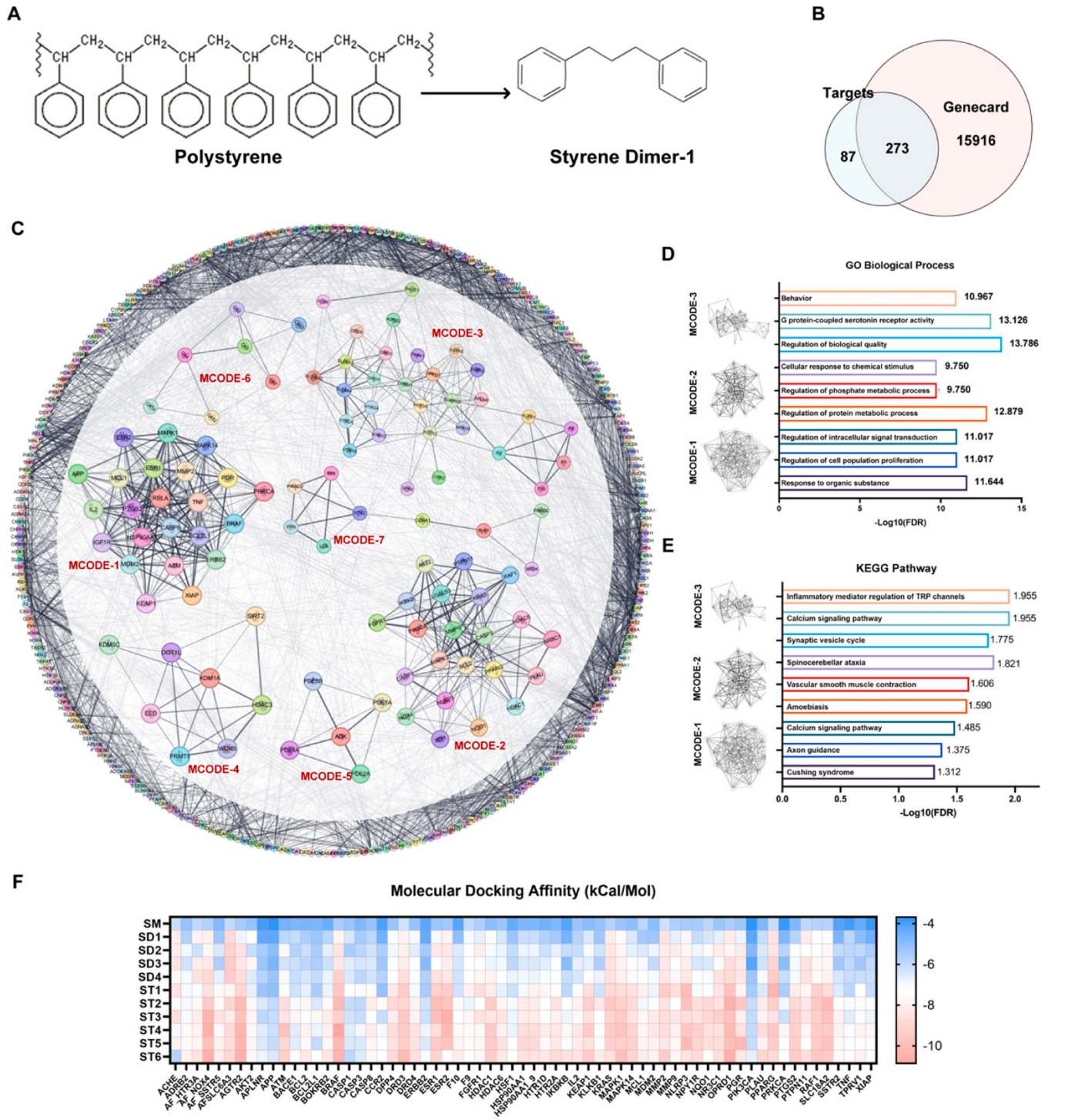

Fig. 2. Overview of the predicted target network and molecular docking results for SD-1. (A) The chemical structure of polystyrene and its degradation into SD-1. (B) Venn diagram illustrating the overlap between the predicted SD-1 targets and neuro-related targets found in GeneCards. (C) Protein-Protein Interaction (PPI) network constructed from the 273 neuro-related SD-1 targets. The network is subdivided into several clusters identified through MCODE analysis. Key clusters, including MCODE-1, MCODE-2, and MCODE-3, are indicated. (D) Gene Ontology (GO) Biological Process enrichment analysis of the top three MCODE clusters, with key processes such as G-protein coupled receptor signaling and calcium ion regulation highlighted.(E) KEGG pathway enrichment analysis of the top three MCODE clusters, identifying pathways involved in calcium signaling, inflammatory mediator regulation, and vascular smooth muscle contraction. (F) Heatmap showing the molecular docking affinity (kCal/mol) of SD-1, other styrene dimers (SD2–SD5), and styrene trimers (ST1–ST6) against proteins from the top three MCODE clusters. Binding affinities lower than −5 kCal/mol suggest strong binding potential, with certain trimers exhibiting even higher affinity than dimers for some targets.

highlight key nodes—those proteins with the greatest influence on network stability and functionality.

Fig. 3A provides an overview of the InfomaxNet architecture. The input is a PPI network comprising interacting proteins. The multi-scale encoder (composed of stacked GCN layers) captures both local and global structural features of the network. These features are then processed through the DGI module, which performs contrastive learning by comparing the original network against a corrupted version to extract

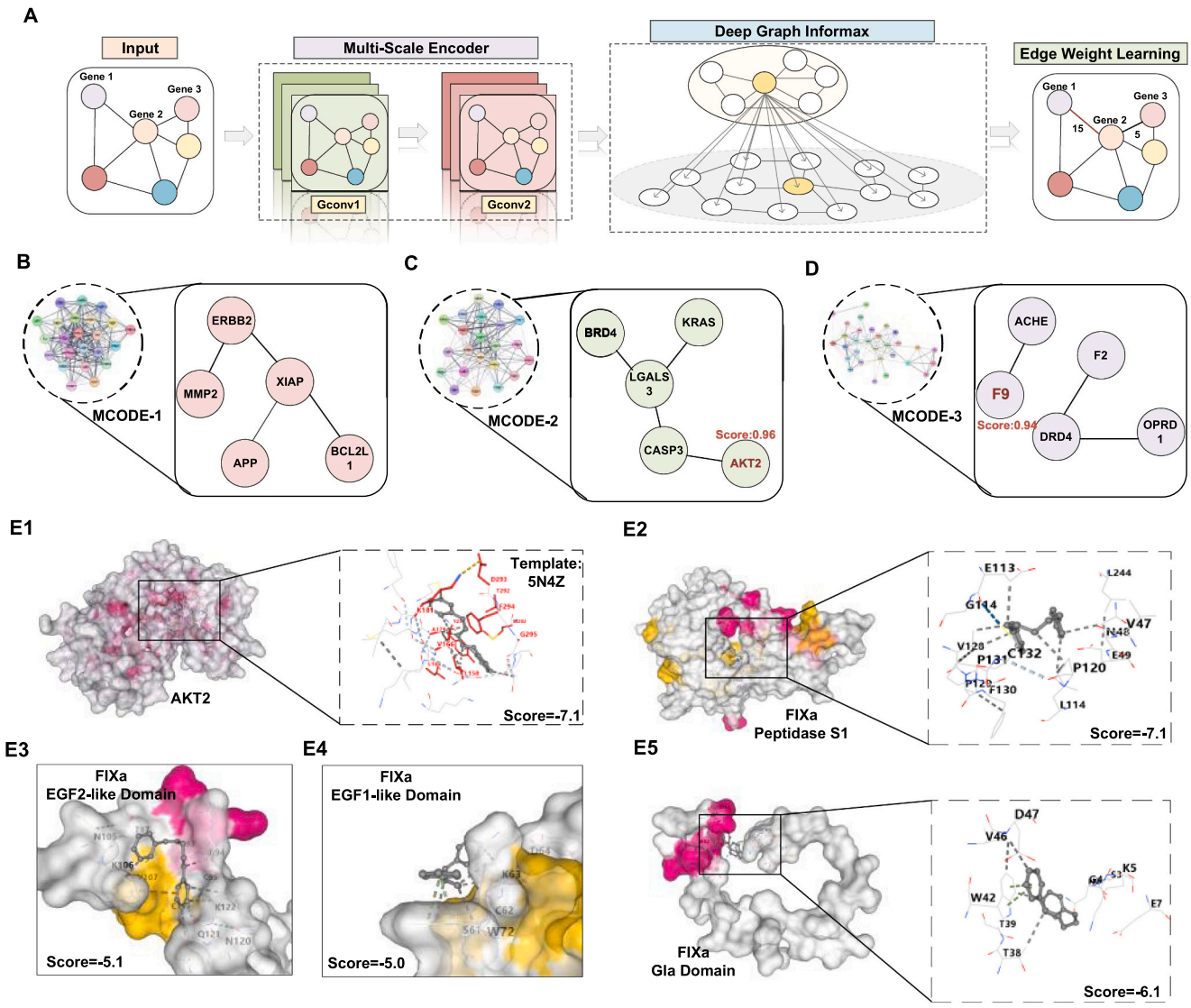

Fig. 3. InfomaxNet Analysis of MCODE Clusters and Molecular Docking Results. (A) The InfomaxNet framework for identifying key proteins in PPI networks, integrating multi-scale graph convolutional encoding, Deep Graph Infomax (DGI), and edge weight learning (EWL). (B–D) Results of InfomaxNet analysis on three MCODE clusters. (E1–E5) Molecular docking simulations between SD-1 and critical domains of AKT2 and F9. (E1) SD-1 interaction with AKT2 reveals a binding affinity of −7.1 kcal/mol. (E2) SD-1 binding to the Peptidase S1 domain of FIXa (F9) with an affinity of −7.1 kcal/mol. (E3–E4) SD-1 interactions with the EGF1-like domain of FIXa show affinities between −5.0 to −5.1 kcal/mol. (E5) SD-1 binding to the Gla domain of FIXa with an affinity of −6.1 kcal/mol, suggesting potential disruptions in F9's function and coagulation pathway.

the network's most informative features. Finally, the EWL module assigns significance scores to individual interactions (edges), further refining the model's ability to identify the most influential proteins.

Through InfomaxNet analysis, we identified key proteins in each MCODE cluster (Fig. 3B–D). Notably, AKT2 and F9 emerged as the most influential proteins, with their scores significantly surpassing those of other proteins. These results suggest that AKT2 and F9 are likely to play crucial roles in mediating the toxicological effects of SD-1.

MCODE-2 Cluster (Fig. 3C) highlights AKT2 with a high importance score of 0.96. AKT2, a serine/threonine kinase, plays a pivotal role in regulating processes like glucose metabolism and apoptosis, making it a prime candidate for investigating SD-1's potential impact on metabolic pathways and cell survival. And MCODE-3 Cluster (Fig. 3D) reveals F9 with a similarly high score of 0.94. F9 (also known as Factor IX) is a key component of the coagulation cascade, responsible for blood clot formation. The disruption of F9's function can lead to coagulation disorders, raising concerns about SD-1's potential to interfere with the normal functioning of the coagulation system.

To further explore the interactions between SD-1 and these key proteins, we performed molecular docking simulations. The results confirmed strong binding affinities between SD-1 and the critical proteins identified in the InfomaxNet analysis.

The docking simulation revealed a high binding affinity of −7.1 kcal/mol between SD-1 and AKT2. This suggests that SD-1 might directly interfere with AKT2's function, potentially disrupting metabolic regulation and promoting cell stress or apoptosis.

We analyzed SD-1's binding interactions with multiple domains of the activated form of F9 (FIXa) to explore its potential effects on coagulation. The docking results revealed a high binding affinity of −7.1 kcal/mol with the Peptidase S1 domain (Fig. E2), indicating a strong interaction that could potentially interfere with the protease activity essential for blood clotting. Additionally, the EGF1-like domain (Fig. E3–E4) exhibited binding affinities ranging between −5.0 to −5.1 kcal/mol, suggesting that SD-1 may disrupt F9's interactions with co-factors or other proteins critical for the clotting cascade. Furthermore, the Gla domain (Fig. E5) showed a moderate binding affinity of

−6.1 kcal/mol, reinforcing the hypothesis that SD-1 impairs F9's normal function, thereby increasing the risk of coagulation disorders.

These findings suggest that AKT2 and F9 are central to the toxicological mechanism of SD-1. AKT2's involvement indicates that SD-1 may interfere with metabolic pathways, potentially triggering oxidative stress or apoptosis. Meanwhile, the disruption of F9's activity raises concerns about SD-1's potential to impair blood coagulation, leading to coagulation disorders.

3.3. Molecular dynamics analysis between FIXa and SD-1

In this section, we focus on FIXa, a key enzyme within the coagulation cascade that plays an essential role in blood clot formation. FIXa catalyzes the activation of Factor X, which in turn leads to thrombin generation and fibrin clot formation (Sheehan, 2021; Østergaard et al., 2021). Although microplastic degradation products such as SD-1 have been extensively studied for their environmental impact, the potential relationship between these chemical by-products and coagulation system dysfunction remains largely unexplored. Understanding this connection is essential for uncovering the broader biological effects of microplastic exposure, especially given the increasing presence of plastic-related pollutants in the environment.

To investigate the potential interaction between SD-1 and FIXa, we conducted a molecular dynamics (MD) simulation of the SD-1-FIXa complex. MD simulations, based on classical Newtonian mechanics, model the movements and interactions of molecules over time by solving Newton's equations of motion. This approach offers detailed insight into molecular behavior under controlled conditions, enabling us to predict toxicological effects and explore mechanisms of action at the molecular level. Additionally, MD simulations provide a cost-efficient and time-saving alternative to traditional animal experiments, promoting the adoption of non-animal toxicity evaluation methods.

We performed a 100-nanosecond (100,000 ps) MD simulation to examine the dynamic behavior of the SD-1-FIXa complex. The structural visualization at different time points reveals significant conformational changes in FIXa, followed by the binding of SD-1 (Fig. 4A1–A3). During the first 31.5 ns of the simulation, FIXa undergoes substantial rearrangements that likely prepare the binding site for interaction with SD-1 (Fig. 4A1–A2). By 70 ns, SD-1 binds to the protein, leading to observable changes at the binding site, which subsequently closes around the ligand (Fig. 4A3). This binding event suggests that SD-1 may interfere with the active site of FIXa, potentially impairing its catalytic function and disrupting the coagulation process.

The stability and flexibility of the protein-ligand complex over time are tracked through the Root Mean Square Deviation (RMSD). After 31.5 ns, fluctuations appear in the RMSD of both the Cα atoms of the protein and the ligand, indicating significant structural adjustments upon ligand binding. This result suggests that SD-1 binding induces dynamic changes within FIXa, realigning the active site to accommodate the ligand effectively.

The Solvent Accessible Surface Area (SASA) initially increases as the protein explores more open conformations, but it gradually decreases after SD-1 binds to the active site. This reduction in SASA indicates that hydrophobic regions within the protein become buried, contributing to the stability of the complex (Raghunathan, 2024; Ali et al., 2014). Meanwhile, the Radius of Gyration (Rg) shows periodic fluctuations, reflecting a "breathing motion" in which the protein alternates between more open and closed states. Although the protein retains some flexibility, the binding site remains stably closed once SD-1 is bound, suggesting that the ligand interaction reinforces the structural integrity of FIXa.

The interaction energy plot reveals sharp fluctuations around 31.5 ns, coinciding with the binding of SD-1 to FIXa. Since SD-1 lacks polar functional groups, it primarily interacts with FIXa through van der Waals forces—specifically Lennard-Jones short-range (LJ-SR) interactions (Qiu et al., 2021; Kiessling, 2023). These interactions are driven by hydrophobic effects, where nonpolar molecules generate temporary dipoles that result in attractive forces, facilitating molecular alignment and binding. This type of interaction is consistent with the nonpolar nature of SD-1, which makes it difficult to form hydrogen bonds or engage in strong Coulombic interactions.

Throughout the simulation, the protein distance dynamics plot shows variations in the distances between key residues of FIXa. The lines representing the maximum and minimum distances reflect dynamic rearrangements within the protein, though the binding site remains securely closed after the interaction with SD-1. The Root Mean Square Fluctuation (RMSF) analysis further reveals that regions surrounding the active site exhibit elevated fluctuations, indicating that SD-1 binding induces conformational shifts in these areas. These shifts suggest that the ligand interaction could alter the functional dynamics of FIXa, potentially impairing its ability to catalyze reactions essential for clotting.

The Gibbs free energy landscape illustrates the most stable conformational states of FIXa, with these stable states—also known as energy wells—corresponding to the closed conformations observed after SD-1 binding (Wang et al., 2021; Moharana et al., 2023). The periodic transitions between these wells indicate that the protein undergoes reversible conformational changes, contributing to the observed breathing motion. Additionally, the residue-residue correlation matrix highlights coordinated motions among residues within FIXa. The interaction of SD-1 with the binding site triggers a cascade of conformational changes that extend to other residues throughout the protein, suggesting that binding-induced perturbations at the active site influence distant regions and potentially affect the protein's catalytic activity.

The MM-PBSA calculations revealed a binding free energy (ΔG) of −8.1 kcal/mol for the SD-1–F9 complex, suggesting moderate-to-strong affinity consistent with the observed functional perturbation of coagulation pathways. To probe the structural basis of this interaction, we performed in silico saturation mutagenesis on four high-RMSF residues (T61, Y79, F134, S204) within the binding pocket, along with a negative-control residue (V16). While V16 mutations showed negligible ΔΔG variations (−0.4 to +0.6 kcal/mol), confirming its minimal energetic role, the high-flexibility residues exhibited striking mutational sensitivity.

In summary, our molecular dynamics analysis reveals that SD-1 binding induces significant structural and energetic changes in FIXa. The interaction, primarily driven by van der Waals forces, results in the closure of the active site and alterations in the protein's dynamic behavior. These findings suggest that SD-1 may interfere with the normal function of FIXa, impairing its participation in the coagulation cascade and potentially increasing the risk of coagulation disorders. This study not only offers valuable insights into the molecular mechanisms underlying SD-1's toxicity but also demonstrates the utility of molecular dynamics simulations in toxicology research, providing a powerful tool for investigating chemical-protein interactions.

3.4. Effect of SD-1 on coagulation pathways through APTT and TEG tests

F9, also known as Factor IX, plays a crucial role in the coagulation cascade by participating in the activation of Factor X, which is essential for thrombin generation and fibrin clot formation. Given the central role of F9 in hemostasis, any compound that interferes with its function could have significant implications for blood coagulation and overall vascular health. To investigate whether SD-1 affects the coagulation pathway involving F9, we conducted a series of in vitro assays, including activated partial thromboplastin time (APTT) tests and thromboelastography (TEG) analyses (Fig. 5A).

The APTT test is a sensitive assay used to evaluate the functionality of the intrinsic and common pathways of coagulation, where F9 is a key component. We assessed the effect of varying concentrations of SD-1 on APTT values to determine if SD-1 influences coagulation times indicative of F9 activity.

Our results demonstrated a dose-dependent effect of SD-1 on APTT

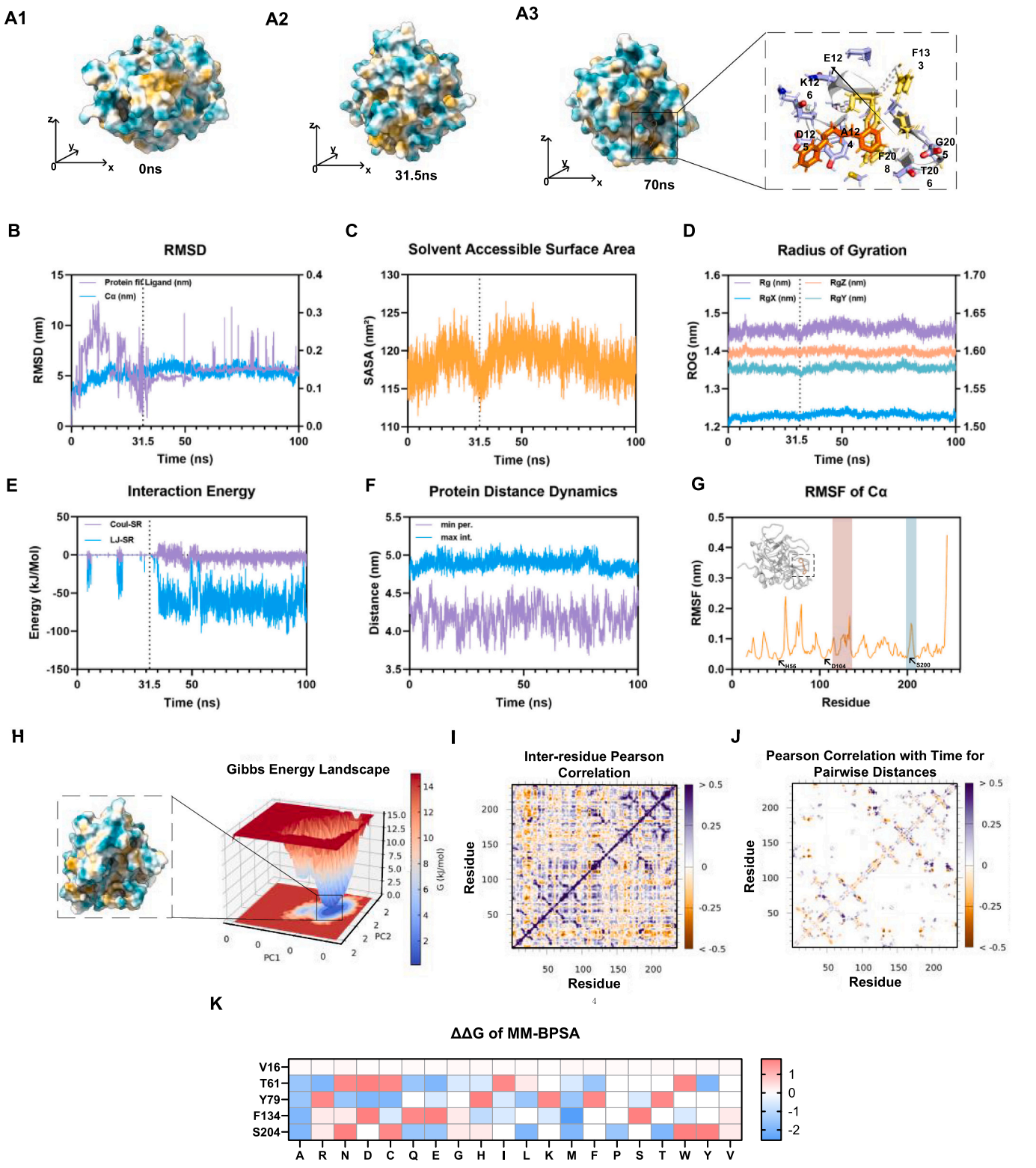

Fig. 4. Molecular Dynamics Analysis of the SD-1-FIXa Complex. (A1–A3) Structural snapshots of FIXa at 0 ns, 31.5 ns, and 70 ns, showing significant conformational changes and binding of SD-1. (B) RMSD plot indicating conformational fluctuations over time. (C) SASA plot showing the reduction in surface area as hydrophobic regions become buried upon ligand binding. (D) Radius of gyration (Rg) plot reflecting the protein's periodic "breathing" motion. (E) Interaction energy plot highlighting van der Waals-driven binding at 31.5 ns. (F) Protein distance dynamics showing rearrangements between key residues. (G) RMSF analysis revealing enhanced flexibility around the active site. (H) Gibbs energy landscape illustrating stable conformational states. (I–J) Residue-residue correlation matrices displaying coordinated motions within FIXa, triggered by SD-1 binding. (K) Binding free energy (ΔG) changes from saturation mutagenesis of high-RMSF residues.

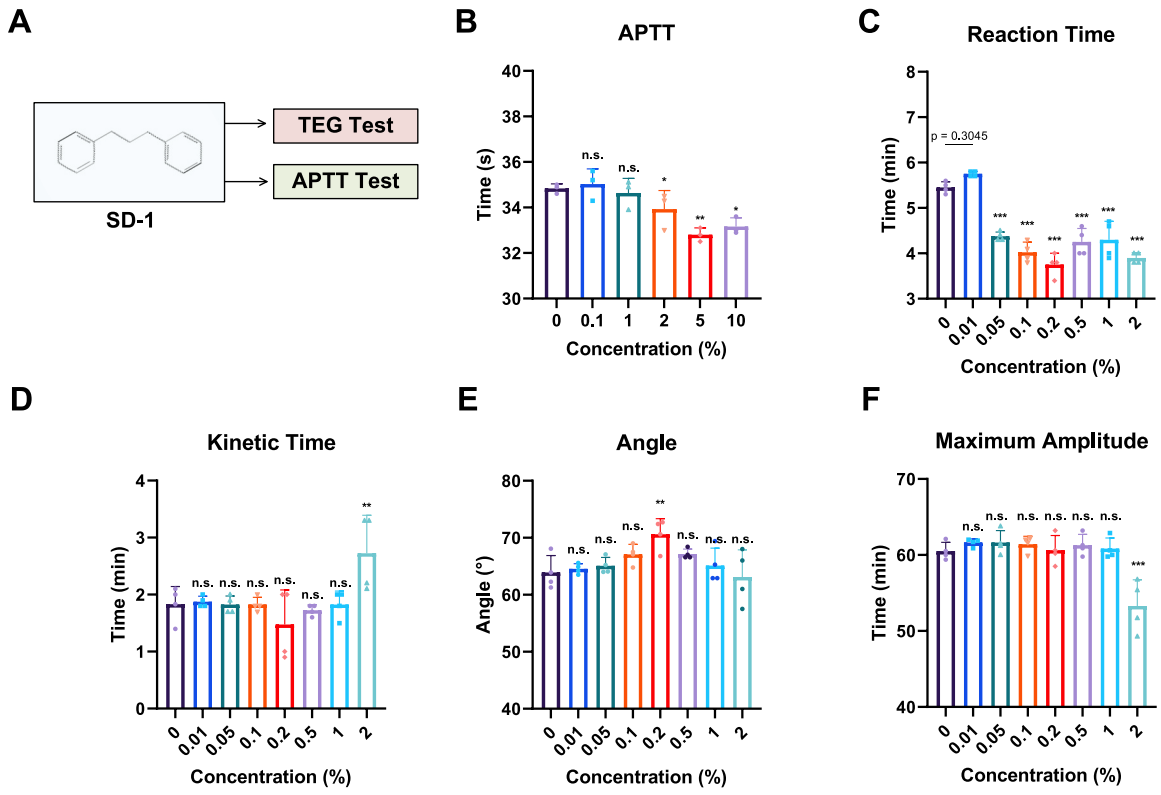

Fig. 5. APTT and TEG Tests Evaluating the Effect of SD-1 on Coagulation Pathways. (A) Schematic representation of the experimental design, including APTT and TEG tests. (B) APTT values across a concentration gradient, showing a decrease followed by a rebound, with significance emerging at 2 % concentration. (C) R time measurements from TEG tests, demonstrating a dose-dependent decrease at low concentrations, with recovery at concentrations beyond 0.2 %. (D) K time remains largely unaffected across the concentration range. (E) The angle shows a mild dose-dependent response, peaking at 0.2 %, though not statistically significant. (F) Maximum amplitude (MA) results, indicating no significant changes in clot strength at low concentrations. $*p < 0.05$, $**p < 0.01$, $***p < 0.001$, n.s. non-significance.

values (Fig. 5B). At lower concentrations (0.1–1 %), SD-1 caused a significant shortening of the APTT compared to the control, suggesting a hypercoagulable state. This initial decrease in APTT implies that SD-1 may enhance the activity of coagulation factors, potentially by increasing the catalytic efficiency of F9 or promoting its activation.

However, at higher concentrations (2 % and above), the APTT values began to increase, approaching or exceeding control levels. This biphasic response suggests that while SD-1 may enhance coagulation at lower concentrations, higher concentrations could inhibit coagulation factors or induce a state of anticoagulation. The rebound in APTT values at higher SD-1 concentrations may be due to inhibitory effects on F9 function or the activation of anticoagulant pathways.

The first significant change in APTT was observed at 2 % concentration, leading us to perform TEG tests within the 0–2 % concentration range to further evaluate SD-1's impact. The TEG tests revealed that SD-1 influences reaction time (R time) at extremely low concentrations (Fig. 5C). R time reflects the time until initial fibrin formation begins, predominantly influenced by coagulation factors in the intrinsic pathway, including F9. Our TEG results showed a significant decrease in R time with increasing concentrations of SD-1 up to 0.2 % (Fig. 5C). This shortening of R time indicates that SD-1 accelerates the initiation of clot formation, supporting the notion that SD-1 enhances F9 activity or promotes its activation.

We observed minimal changes in kinetic time (K time), which represents the time required for clot strength to build up (Fig. 5D). The results imply that SD-1 does not significantly impact the rate of clot development. However, SD-1 did show a slight effect on the angle, which measures the speed of fibrin accumulation and clot strengthening (Fig. 5E). At 0.2 % concentration, the angle displayed a mild dose-dependent response, suggesting a subtle modulation in fibrin formation, although not statistically significant.

Lastly, SD-1 exhibited minimal effects on maximum amplitude (MA), which reflects the final clot strength (Fig. 5F). The lack of significant change in MA at low concentrations indicates that SD-1 has limited influence on the mechanical properties of the formed clot. These findings suggest that while SD-1 affects the early stages of clot initiation, its impact on overall clot integrity remains minimal at the tested concentrations.

In summary, the combined findings from the APTT and TEG assays indicate that SD-1 influences the coagulation process, particularly affecting the initiation phase where F9 plays a pivotal role. The shortening of APTT and R time at lower SD-1 concentrations suggests that SD-1 may enhance F9 activity or facilitate its activation, leading to a pro-coagulant effect.

The biphasic response observed in the APTT assay, with APTT values increasing at higher SD-1 concentrations, may reflect a complex interaction where SD-1 begins to inhibit coagulation factors or activate anticoagulant mechanisms when present at elevated levels. This could be due to SD-1 inducing conformational changes in F9 that, beyond a certain concentration threshold, impair its function rather than enhance it.

Our molecular dynamics simulations provide a mechanistic basis for these observations. The simulations revealed that SD-1 binds to the active site of FIXa (activated F9), inducing conformational changes that could alter its enzymatic activity. At lower concentrations, SD-1 may bind in a manner that stabilizes the active conformation of FIXa, enhancing its catalytic efficiency and leading to a pro-coagulant effect. Conversely, at higher concentrations, excessive binding of SD-1 could disrupt the active site's configuration, hindering substrate access or catalytic function, thereby exerting an anticoagulant effect.

3.5. Impact of SD-1 on the AKT-2 Pathway in C. elegans

To confirm that SD-1 influences the pathway involving AKT-2, we constructed the protein-protein interaction (PPI) network centered around AKT-2 (Fig. 6A). If SD-1 targets AKT-2, it is reasonable to expect downstream genes within this network to exhibit altered expression. To explore this hypothesis, we conducted an acute toxicity assay to determine a suitable concentration for chronic toxicity testing.

The acute toxicity assay revealed that SD-1 induces 21.43 % mortality at a concentration as low as 0.01 % (Fig. 6B). We calculated the LC25 (lethal concentration for 25 % of organisms) to be approximately 0.1 %. Based on this, we selected 0.01 % SD-1 (1/10th of LC25) for chronic exposure experiments. After treating *C. elegans* from the L4 stage for two days, we performed RT-qPCR analysis to assess the expression of AKT-2-related genes.

Our results indicate that exposure to SD-1 (0.01 %) on L4 worm for 2 days led to significant changes in gene expression within the AKT-2 pathway (Fig. 6C), while a notable toxic endpoint such as reduced locomotion—was observed. Specifically, *let-363* and *aap-1* were upregulated, while *age-1* and *rict-1* were downregulated.

The gene *let-363* (mTOR) plays a central role in cellular growth, metabolism, and protein synthesis (Smith et al., 2023). Its upregulation suggests that the AKT-2 pathway might be driving increased metabolic activity or promoting cell growth, possibly as a compensatory response to stress induced by SD-1 exposure (Cheng et al., 2023). The increased expression of *let-363* aligns with the idea that the organism may attempt to counterbalance SD-1 toxicity by enhancing cellular processes to maintain homeostasis.

And *aap-1* (PI3K adaptor protein) is essential for transducing signals from insulin-like receptors to AKT-2 (Wolkow et al., 2002), facilitating the activation of downstream metabolic processes (Houthoofd et al., 2005; Li et al., 2014). The upregulation of *aap-1* following SD-1 exposure could reflect an attempt by the cell to enhance signaling through the insulin/IGF-1 pathway, possibly to restore metabolic balance in the face of external chemical stress. This heightened signaling could explain the upregulation of *let-363*, promoting survival mechanisms despite toxic challenges.

In contrast, *age-1* (PI3K catalytic subunit), a key gene upstream of AKT-2, was downregulated. This unexpected reduction could indicate feedback inhibition within the insulin signaling pathway to prevent overactivation. Prolonged activation of AKT-2 or related pathways can result in negative regulatory mechanisms, reducing upstream PI3K activity to maintain cellular equilibrium. The downregulation of *age-1* suggests that although AKT-2 is active, the system may be preventing excessive PI3K activation to avoid cellular damage or metabolic imbalance.

Similarly, *rict-1* (part of mTORC2 complex), involved in cytoskeletal organization and AKT-2 activation, was also downregulated. This could be an adaptive response to mitigate cellular stress and prevent overactivation of AKT-2-dependent pathways (Ruf et al., 2013; Emans et al., 2023; Webster et al., 2013). Downregulation of *rict-1* might reduce AKT-2 phosphorylation, curbing excessive metabolic activity to protect against damage caused by SD-1.

In summary, these results suggest that SD-1 may act as a modulator of AKT-2, promoting selective activation and repression within the insulin/IGF-1 signaling network (Qi et al., 2021). This dual regulatory

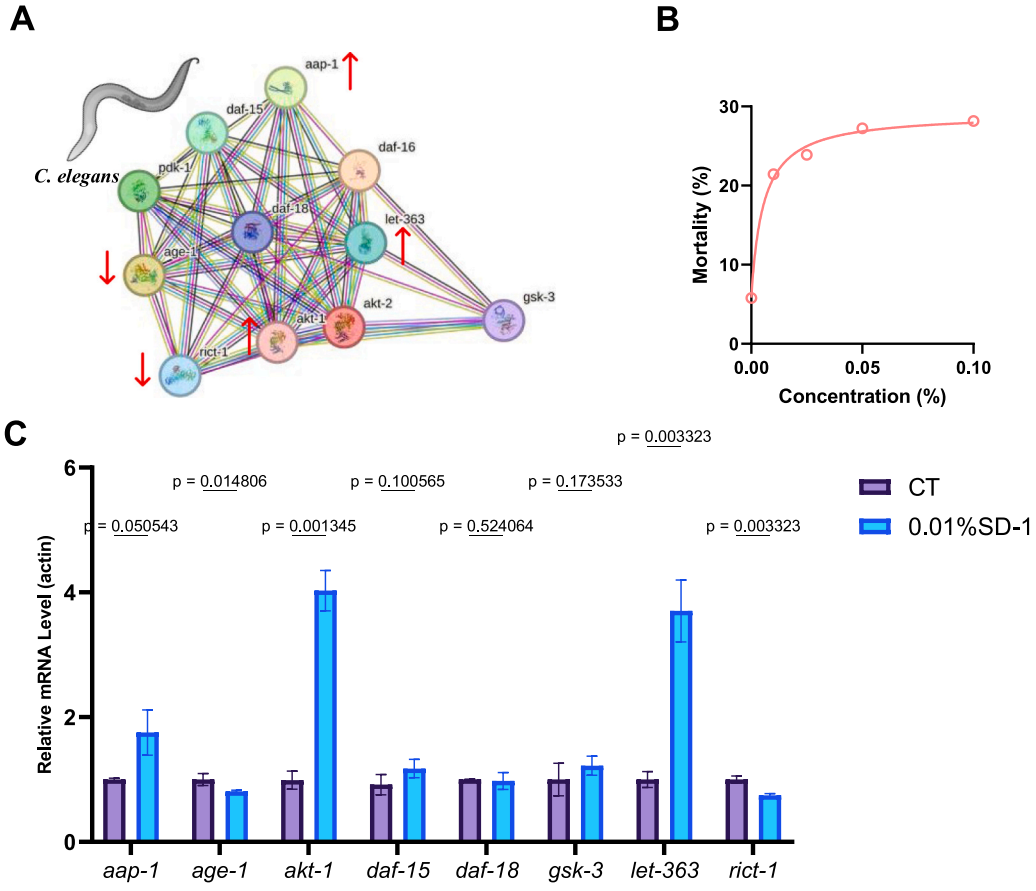

Fig. 6. AKT-2 Pathway and the Impact of SD-1 on Gene Expression in *C. elegans*. (A) PPI network centered around AKT-2, illustrating interactions with related genes involved in the insulin/IGF-1 signaling pathway. Red arrows indicate upregulation, and downward arrows indicate downregulation of expression in response to SD-1. (B) Mortality curve from the acute toxicity assay. (C) RT-qPCR results displaying relative mRNA levels of key genes in the AKT-2 pathway after exposure to 0.01 % SD-1.

effect likely reflects an attempt to maintain cellular balance and protect against toxicity induced by SD-1. Such modulation could have significant implications for the regulation of growth, metabolism, and lifespan, as AKT-2 plays a crucial role in these processes. The altered gene expression pattern indicates that SD-1 disrupts normal signaling dynamics, potentially impairing the organism's ability to adapt to environmental stressors and maintain physiological homeostasis. Further investigations are warranted to elucidate the precise binding interactions between SD-1 and AKT-2 and to explore the long-term physiological impacts of this disruption.

3.6. Alignment with global trends in ecotoxicology

Recent advances in ecotoxicology emphasize mechanistic toxicology, the integration of omics-based approaches, and the application of in silico modeling techniques to uncover toxic effects at the molecular and systems level. In this context, the InfomaxNet framework proposed here represents a significant step forward in computational toxicology, as it addresses the challenge of lacking prior biological knowledge by relying solely on the network topology of predicted protein targets.

Environmental exposure to plastic degradation products, especially micro- and nanoplastics, has become a pressing concern worldwide. Compounds such as SD-1, which can leach from polystyrene-based materials, have been detected in various environmental matrices including soil, freshwater, and even food-contact surfaces (Megill et al., 2024; Zhang et al., 2023; Rowdhwal and Chen, 2018). However, their toxicological profiles remain largely underexplored. By identifying coagulation disorder as a key adverse outcome of SD-1 exposure and revealing F9 and AKT2 as critical molecular targets, this study addresses a significant knowledge gap and provides a mechanistic basis for understanding the health and ecological risks posed by such compounds. It contributes to the global effort of mechanistic hazard assessment of plastic-related pollutants and demonstrates how integrative modeling can enhance the predictive power of ecotoxicological frameworks.

4. Conclusion

This study systematically explored the toxicological mechanisms of 1,3-diphenylpropane (SD-1) using a combination of network toxicology with a new framework 'InformaxNet' which successfully addresses the challenge of lacking prior biological knowledge in network analysis, molecular dynamics simulations, in vitro coagulation assays, and *C. elegans* experiments. Our results reveal that SD-1 disrupts biological processes by targeting key proteins such as AKT-2 and F9, impairing their normal functions. InfomaxNet analysis identified these proteins as central to the metabolic and coagulation pathways, with SD-1 binding to AKT2 influencing insulin/IGF-1 signaling and interfering with F9 (FIXa) to impair coagulation function. Molecular dynamics simulations confirmed that SD-1 binding induces conformational changes in FIXa, potentially increasing the risk of coagulation disorders. Meanwhile, toxicity assays in *C. elegans* further validated the regulatory impact of SD-1 on AKT-2 and its downstream genes.

Together, these findings highlight the potential health risks posed by SD-1 through the disruption of critical biological pathways, offering new insights into the toxic mechanisms of polystyrene by-products. This research not only advances the understanding of SD-1 toxicity but also provides a replicable framework for evaluating the toxic effects of emerging pollutants through deep learning-based network toxicology and molecular simulations.

CRediT authorship contribution statement

Lei Cheng: Writing – review & editing, Data curation. **Juan Long:** Supervision, Resources, Methodology. **Wenjing Zhang:** Writing – original draft, Validation, Software. **Nan Zhang:** Writing – review & editing, Validation, Resources, Investigation. **Guojun Li:** Writing – review & editing, Writing – original draft, Project administration, Methodology, Funding acquisition. **Hongxia Cai:** Supervision, Methodology, Data curation. **Bo Xian:** Writing – review & editing, Resources, Project administration, Methodology, Funding acquisition, Conceptualization. **Yufeng Ran:** Resources, Methodology, Data curation. **Shan Gao:** Resources, Funding acquisition. **Xiaowei Qiu:** Supervision, Resources, Methodology. **Yan Pan:** Writing – original draft, Methodology, Data curation, Conceptualization. **Hexiang Qiu:** Writing – review & editing, Visualization, Validation, Formal analysis. **Zhihang Huang:** Writing – review & editing, Visualization, Methodology. **Dan Wu:** Writing – review & editing, Visualization, Validation.

Consent for publication

Not applicable.

Ethics approval and consent to participate

This study received approval from the Ethical Committee of the University of Electronic Science and Technology of China, Chengdu, China (Ethics Approval No. 106142025022332068). Informed consent was obtained from all human participants prior to the collection of blood samples. All procedures performed in this study adhered to the ethical standards of the institutional and national research committee and complied with the 1964 Helsinki Declaration and its later amendments.

Funding

This research was supported in part by the 2021 Research Start-up Fund Fresh Wave (Central Finance Special, Grant No. Y030212059003033 to B.X.), the Leading Principal Investigator of Beijing High-level Public Health Technical Talents Construction Project (Grant No.02-03 to G.L.).

Declaration of Competing Interest

The authors declare that they have no known competing financial interests or personal relationships that could have appeared to influence the work reported in this paper.

Acknowledgments

Special thanks to Prof. Jau-Shyong (John) Hong for his invaluable advice on experimental design and Ms. Nature Belle and Ms. Jiexin Zheng for their assistance. We also extend our appreciation to Aging laboratory technicians for their diligent work in maintaining the *C. elegans* cultures and to the administrative staff for their support throughout the project. Furthermore, we would like to express our gratitude to UESTC_BioMed for their revisions of the figures and language in this manuscript.

Appendix A. Supporting information

Supplementary data associated with this article can be found in the online version at doi:10.1016/j.ecoenv.2025.118834.

Data availability

all codes and data will be published at https://github.com/Marissapy.

References

Ajaj, A., J'Bari, S., Ononogbo, A., Buonocore, F., Bear, J.C., Mayes, A.G., Morgan, H., 2021. An insight into the growing concerns of styrene monomer and Poly(Styrene) fragment migration into food and drink simulants from Poly(Styrene) packaging.

Foods 10 (5), 1136. https://doi.org/10.3390/foods10051136. PMID: 34065221; PMCID: PMC8160766.
Ali, S.A., Hassan, M.I., Islam, A., Ahmad, F., 2014. A review of methods available to estimate solvent-accessible surface areas of soluble proteins in the folded and unfolded states. Curr. Protein Pept. Sci. 15 (5), 456–476. https://doi.org/10.2174/1389203715666140327114232. PMID: 24678666.
Arancibia, P.A., Morin, P.J., 2022. Network topology and patch connectivity affect dynamics in experimental and model metapopulations. J. Anim. Ecol. 91 (2), 496–505. https://doi.org/10.1111/1365-2656.13647. Epub 2021 Dec 19. PMID: 34873688.
Beneventi, E., Goldbeck, C., Zellmer, S., Merkel, S., Luch, A., Tietz, T., 2022. Migration of styrene oligomers from food contact materials: in silico prediction of possible genotoxicity. Arch. Toxicol. 96 (11), 3013–3032. https://doi.org/10.1007/s00204-022-03350-x. Epub 2022 Aug 13. PMID: 35963937; PMCID: PMC9376037.
Bessadok, A., Mahjoub, M.A., Rekik, I., 2023. Graph neural networks in network neuroscience. IEEE Trans. Pattern Anal. Mach. Intell. 45 (5), 5833–5848. https://doi.org/10.1109/TPAMI.2022.3209686. Epub 2023 Apr 3. PMID: 36155474.
Bianchi, F.M., Grattarola, D., Livi, L., Alippi, C., 2022. Graph neural networks with convolutional ARMA filters. IEEE Trans. Pattern Anal. Mach. Intell. 44 (7), 3496–3507. https://doi.org/10.1109/TPAMI.2021.3054830. Epub 2022 Jun 3. PMID: 33497331.
Cheng, X., Zhang, P., Zhao, H., Zheng, H., Zheng, K., Zhang, H., Zhang, H., 2023. Proteotoxic stress disrupts epithelial integrity by inducing MTOR sequestration and autophagy overactivation. Autophagy 19 (1), 241–255. https://doi.org/10.1080/15548627.2022.2071381. Epub 2022 May 6. PMID: 35521960; PMCID: PMC9809964.
Del Giudice, G., Serra, A., Pavel, A., Torres Maia, M., Saarimäki, L.A., Fratello, M., Federico, A., Alenius, H., Fadeel, B., Greco, D., 2024. A network toxicology approach for mechanistic modelling of nanomaterial hazard and adverse outcomes. Adv. Sci. 11 (32), e2400389. https://doi.org/10.1002/advs.202400389. Epub 2024 Jun 25. PMID: 38923832; PMCID: PMC11348149.
Emans, S.W., Yerevanian, A., Ahsan, F.M., Rotti, J.F., Zhou, Y., Cedillo, L., Soukas, A.A., 2023. GRD-1/PTR-11, the C. Elegans hedgehog/patched-like morphogen-receptor pair, modulates developmental rate. Development 150 (24), dev201974. https://doi.org/10.1242/dev.201974. Epub 2023 Dec 11. PMID: 37982457; PMCID: PMC10753586.
Hong, S., Lee, J., Lee, C., Yoon, S.J., Jeon, S., Kwon, B.O., Lee, J.H., Giesy, J.P., Khim, J. S., 2016. Are styrene oligomers in coastal sediments of an industrial area aryl hydrocarbon-receptor agonists? Environ. Pollut. 213, 913–921. https://doi.org/10.1016/j.envpol.2016.03.025. Epub 2016 Apr 1. PMID: 27043777.
Houthoofd, K., Fidalgo, M.A., Hoogewijs, D., Braeckman, B.P., Lenaerts, I., Brys, K., Matthijssens, F., De Vreese, A., Van Eygen, S., Muñoz, M.J., Vanfleteren, J.R., 2005. Metabolism, physiology and stress defense in three aging Ins/IGF-1 mutants of the nematode caenorhabditis elegans. Aging Cell 4 (2), 87–95. https://doi.org/10.1111/j.1474-9726.2005.00150.x. PMID: 15771612.
Huang, S., 2024. Analysis of environmental pollutant bisphenol f elicited prostate injury targets and underlying mechanisms through network toxicology, molecular docking, and multi-level bioinformatics data integration. Toxicology 506, 153847. https://doi.org/10.1016/j.tox.2024.153847. Epub 2024 Jun 2. PMID: 38830480.
Kiessling, M.K., 2023. Testing Lennard-Jones clusters for optimality. J. Chem. Phys. 159 (1), 014301. https://doi.org/10.1063/5.0158931. PMID: 37409703.
Kriegeskorte, N., Golan, T., 2019. Neural network models and deep learning. Curr. Biol. 29 (7), R231–R236. https://doi.org/10.1016/j.cub.2019.02.034. PMID: 30939301.
Li, F.C., Gasser, R.B., Lok, J.B., Korhonen, P.K., Wang, Y.F., Yin, F.Y., He, L., Zhou, R., Zhao, J.L., Hu, M., 2014. Exploring the role of two interacting phosphoinositide 3-kinases of haemonchus contortus. Parasit. Vectors 7, 498. https://doi.org/10.1186/s13071-014-0498-2. PMID: 25388625; PMCID: PMC4233088.
Liu, H., He, L., Zhang, F., Wang, Z., Gao, C., 2022b. Dynamic community detection over evolving networks based on the optimized deep graph infomax. Chaos 32 (5), 053119. https://doi.org/10.1063/5.0086795. PMID: 35650000.
Liu, Z., Sokratian, A., Duda, A.M., Xu, E., Stanhope, C., Fu, A., Strader, S., Li, H., Yuan, Y., Bobay, B.G., Sipe, J., Bai, K., Lundgaard, I., Liu, N., Hernandez, B., Bowes Rickman, C., Miller, S.E., West, A.B., 2023a. Anionic nanoplastic contaminants promote parkinson's disease-associated α-synuclein aggregation. Sci. Adv. 9 (46), eadi8716. https://doi.org/10.1126/sciadv.adi8716. Epub 2023 Nov 17. PMID: 37976362; PMCID: PMC10656074.
Liu, Z., Sokratian, A., Duda, A.M., Xu, E., Stanhope, C., Fu, A., Strader, S., Li, H., Yuan, Y., Bobay, B.G., Sipe, J., Bai, K., Lundgaard, I., Liu, N., Hernandez, B., Rickman, C.B., Miller, S.E., West, A.B., 2023b. Anionic nanoplastic contaminants promote parkinson's Disease-Associated α-Synuclein aggregation. Res Sq. [Prepr.], rs-3439102. https://doi.org/10.21203/rs.3.rs-3439102/v1. Update in: Sci Adv. 2023 Nov 15;9(46):eadi8716. doi: 10.1126/sciadv.adi8716. PMID: 37886561; PMCID: PMC10602106.
Liu, M., Wang, Z., Ji, S., 2022a. Non-Local graph neural networks. IEEE Trans. Pattern Anal. Mach. Intell. 44 (12), 10270–10276. https://doi.org/10.1109/TPAMI.2021.3134200. Epub 2022 Nov 7. PMID: 34882549.
Megill, C., Shaw, K., Knauer, K., Seeley, M., Lynch, J., 2024. Plastic additives in the ocean: use of a comprehensive dataset for meta-analysis and method development. Chemosphere 358, 142172. https://doi.org/10.1016/j.chemosphere.2024.142172. Epub 2024 Apr 27. PMID: 38685322.
Moharana, M., Pattanayak, S.K., Khan, F., 2023. Molecular recognition of bio-active triterpenoids from *swertia chirayita* towards hepatitis delta antigen: a mechanism through docking, dynamics simulation, gibbs free energy landscape. J. Biomol. Struct. Dyn. 41 (24), 14651–14664. https://doi.org/10.1080/07391102.2023.2184173. Epub 2023 Mar 1. PMID: 36856037.
Momennejad, I., 2022. Collective minds: social network topology shapes collective cognition. Philos. Trans. R. Soc. Lond. B Biol. Sci. 377 (1843), 20200315. https://doi.org/10.1098/rstb.2020.0315. Epub 2021 Dec 13. PMID: 34894735; PMCID: PMC8666914.
Morandi, M.I., Kluzek, M., Wolff, J., Schroder, A., Thalmann, F., Marques, C.M., 2021. Accumulation of styrene oligomers alters lipid membrane phase order and miscibility. Proc. Natl. Acad. Sci. USA 118 (4), e2016037118. https://doi.org/10.1073/pnas.2016037118. PMID: 33468682; PMCID: PMC7848699.
Morgan, J.P., Paiement, A., Klinke, C., 2023. Domain-informed graph neural networks: a quantum chemistry case study. Neural Netw. 165, 938–952. https://doi.org/10.1016/j.neunet.2023.06.030. Epub 2023 Jul 1. PMID: 37453397.
Nakai, M., Tsubokura, M., Suzuki, M., Fujishima, S., Watanabe, Y., Hasegawa, Y., Oyama, K., Ogura, S., 2014 Nov 15. Genotoxicity of styrene oligomers extracted from polystyrene intended for use in contact with food. Toxicol. Rep. 1, 1175–1180. https://doi.org/10.1016/j.toxrep.2014.11.007. PMID: 28962327; PMCID: PMC5598101.
Østergaard, H., Lund, J., Greisen, P.J., Kjellev, S., Henriksen, A., Lorenzen, N., Johansson, E., Røder, G., Rasch, M.G., Johnsen, L.B., Egebjerg, T., Lund, S., Rahbek-Nielsen, H., Gandhi, P.S., Lamberth, K., Loftager, M., Andersen, L.M., Bonde, A.C., Stavenuiter, F., Madsen, D.E., Li, X., Holm, T.L., Ley, C.D., Thygesen, P., Zhu, H., Zhou, R., Thorn, K., Yang, Z., Hermit, M.B., Bjelke, J.R., Hansen, B.G., Hilden, I., 2021. A factor VIIIa-mimetic bispecific antibody, Mim8, ameliorates bleeding upon severe vascular challenge in hemophilia a mice. Blood 138 (14), 1258–1268. https://doi.org/10.1182/blood.2020010331. PMID: 34077951; PMCID: PMC8499050.
Qi, Z., Ji, H., Le, M., Li, H., Wieland, A., Bauer, S., Liu, L., Wink, M., Herr, I., 2021. Sulforaphane promotes *c. elegans* longevity and healthspan via DAF-16/DAF-2 insulin/IGF-1 signaling. Aging (Albany NY) 13 (2), 1649–1670. https://doi.org/10.18632/aging.202512. Epub 2021 Jan 20. PMID: 33471780; PMCID: PMC7880325.
Qiu, Y., Shan, W., Zhang, H., 2021. Force field benchmark of amino acids. 3. hydration with scaled Lennard-Jones interactions. J. Chem. Inf. Model 61 (7), 3571–3582. https://doi.org/10.1021/acs.jcim.1c00339. Epub 2021 Jun 29. PMID: 34185520.
Raghunathan, S., 2024. Solvent accessible surface area-assessed molecular basis of osmolyte-induced protein stability. RSC Adv. 14 (34), 25031–25041. https://doi.org/10.1039/d4ra02576h. PMID: 39131493; PMCID: PMC11310836.
Rowdhwal, S.S.S., Chen, J., 2018. Toxic effects of Di-2-ethylhexyl phthalate: an overview. Biomed. Res. Int. 2018, 1750368. https://doi.org/10.1155/2018/1750368. PMID: 29682520; PMCID: PMC5842715.
Ruf, V., Holzem, C., Peyman, T., Walz, G., Blackwell, T.K., Neumann-Haefelin, E., 2013. TORC2 signaling antagonizes SKN-1 to induce C. Elegans mesendodermal embryonic development. Dev. Biol. 384 (2), 214–227. https://doi.org/10.1016/j.ydbio.2013.08.011. Epub 2013 Aug 20. PMID: 23973804; PMCID: PMC3877771.
Ruiz-Garcia, A., Schmidhuber, J., Palade, V., Took, C.C., Mandic, D., 2021. Deep neural network representation and generative adversarial learning. Neural Netw. 139, 199–200. https://doi.org/10.1016/j.neunet.2021.03.009. Epub 2021 Mar 9. PMID: 33774356.
Sheehan, J.P., 2021. Mapping the zymogen to protease transition in FIXa. J. Thromb. Haemost. 19 (6), 1409–1411. https://doi.org/10.1111/jth.15286. PMID: 34047009.
Sludds, A., Bandyopadhyay, S., Chen, Z., Zhong, Z., Cochrane, J., Bernstein, L., Bunandar, D., Dixon, P.B., Hamilton, S.A., Streshinsky, M., Novack, A., Baehr-Jones, T., Hochberg, M., Ghobadi, M., Hamerly, R., Englund, D., 2022. Delocalized photonic deep learning on the Internet's edge. Science 378 (6617), 270–276. https://doi.org/10.1126/science.abq8271. Epub 2022 Oct 20. PMID: 36264813.
Smith, H.J., Lanjuin, A., Sharma, A., Prabhakar, A., Nowak, E., Stine, P.G., Sehgal, R., Stojanovski, K., Towbin, B.D., Mair, W.B., 2023. Neuronal mTORC1 inhibition promotes longevity without suppressing anabolic growth and reproduction in C. Elegans. PLoS Genet. 19 (9), e1010938. https://doi.org/10.1371/journal.pgen.1010938. PMID: 37721956; PMCID: PMC10538657.
Tian, Z., Kim, S.K., Hyun, J.H., 2020. Environmental distribution of styrene oligomers (SOs) coupled with their source characteristics: tracing the origin of SOs in the environment. J. Hazard. Mater. 398, 122968. https://doi.org/10.1016/j.jhazmat.2020.122968. Epub 2020 May 26. PMID: 32768830.
Veličković, P., 2023. Everything is connected: graph neural networks. Curr. Opin. Struct. Biol. 79, 102538. https://doi.org/10.1016/j.sbi.2023.102538. Epub 2023 Feb 9. PMID: 36764042.
Wang, Y., Tang, Z., Chen, H.Y., Wang, W., Tao, N., Wang, H., 2021. Single-molecule calorimeter and free energy landscape. Proc. Natl. Acad. Sci. USA 118 (23), e2104598118. https://doi.org/10.1073/pnas.2104598118. PMID: 34074791; PMCID: PMC8201985.
Webster, C.M., Wu, L., Douglas, D., Soukas, A.A., 2013. A non-canonical role for the C. Elegans dosage compensation complex in growth and metabolic regulation downstream of TOR complex 2. Development 140 (17), 3601–3612. https://doi.org/10.1242/dev.094292. Epub 2013 Jul 24. PMID: 23884442; PMCID: PMC3742143.
Wolkow, C.A., Muñoz, M.J., Riddle, D.L., Ruvkun, G., 2002. Insulin receptor substrate and p55 orthologous adaptor proteins function in the caenorhabditis elegans daf-2/insulin-like signaling pathway. J. Biol. Chem. 277 (51), 49591–49597. https://doi.org/10.1074/jbc.M207866200. Epub 2002 Oct 18. PMID: 12393910.
Wu, Z., Pan, S., Chen, F., Long, G., Zhang, C., Yu, P.S., 2021. A comprehensive survey on graph neural networks. IEEE Trans. Neural Netw. Learn Syst. 32 (1), 4–24. https://doi.org/10.1109/TNNLS.2020.2978386. Epub 2021 Jan 4. PMID: 32217482.
Xiao, S., Lin, H., Wang, C., Wang, S., Rajapakse, J.C., 2023. Graph neural networks with multiple prior knowledge for Multi-Omics data analysis. IEEE J. Biomed. Health Inf. 27 (9), 4591–4600. https://doi.org/10.1109/JBHI.2023.3284794. Epub 2023 Sep 6. PMID: 37307177.
Zhang, Q.Q., Lan, M.Y., Li, H.R., Qiu, S.Q., Guo, Z., Liu, Y.S., Zhao, J.L., Ying, G.G., 2023. Plastic pollution from takeaway food industry in China. Sci. Total Environ. 904,

166933. https://doi.org/10.1016/j.scitotenv.2023.166933. Epub 2023 Sep 12. PMID: 37709096.

Zhao, Z., Du, J.F., Wang, Q.L., Qiu, F.N., Chen, X.Y., Liu, F.J., Li, P., Jiang, Y., Li, H.J., 2023. An integrated strategy combining network toxicology and feature-based molecular networking for exploring hepatotoxic constituents and mechanism of epimedii Folium-induced hepatotoxicity in vitro. Food Chem. Toxicol. 176, 113785. https://doi.org/10.1016/j.fct.2023.113785. Epub 2023 Apr 18. PMID: 37080529.

Zhihang, H., Ezemaduka, A.N., Hongxia, C., Yan, P., Yiwen, G., Nan, Z., Xinrui, L., Shan, G., Guojun, L., Jing, Y., Bo, X., 2024. The joint toxicity effect of glyphosate and cadmium in a concentration-dependent manner on nematode caenorhabditis elegans. Ecotoxicol. Environ. Saf. 285, 117081. https://doi.org/10.1016/j.ecoenv.2024.117081. Epub 2024 Sep 27. PMID: 39341135.

Zhou, Z., Hu, Y., Zhang, Y., Chen, J., Cai, H., 2023. Multiview deep graph infomax to achieve unsupervised graph embedding. IEEE Trans. Cyber 53 (10), 6329–6339. https://doi.org/10.1109/TCYB.2022.3163721. Epub 2023 Sep 15. PMID: 35427229.